CHEMISTRY OF MATERIALS
Cite This: Chem. Mater. 2019, 31, 8473−8483
Article
pubs.acs.org/cm

Designed Synthesis and Structure−Property Relationships of Kinetically Stable $[(PbSe)_{1+\delta}]_m(VSe_2)_1$ (m = 1, 2, 3, 4) Heterostructures

Dmitri Leo Mesoza Cordova,[†] Shannon Sanaya Fender,[†] Taryn Meiko Kam,[†] Johannes Seyd,[‡] Manfred Albrecht,[‡] Ping Lu,[§] Robert Fischer,[†] and David C. Johnson*[,†]

[†]Department of Chemistry and Materials Science Institute, University of Oregon, Eugene, Oregon 97403, United States
[‡]Institut für Physik, Universität Augsburg, Augsburg 86159, Germany
[§]Sandia National Laboratories, Albuquerque, New Mexico 87185, United States

Supporting Information

ABSTRACT: Understanding structure−function relationships is essential to guide the designed synthesis of novel materials with emergent properties. In this work, we targeted the metastable heterostructures $[(PbSe)_{1+\delta}]_m(VSe_2)_1$, where m = 1−4, to test if the charge density wave (CDW) transition temperature increases as the layer thickness separating the VSe_2 monolayers increases, as was observed when SnSe was the separating layer. The modulated elemental reactant approach was used to make the targeted products. This approach involves depositing elemental layers in which the number of atoms of each element per square angstrom in PbISe and VI Se bilayers equals the number calculated for a rock salt-structured PbSe bilayer and a CdI_2-structured VSe_2 slab, respectively. Layered elemental precursors with the correct composition and nanoarchitecture for each of the targeted compounds were prepared by repeatedly depositing a single VISe bilayer followed by m PbISe bilayers. Precursors close to the targeted number of atoms per unit area were determined via X-ray fluorescence and the correct nanoarchitecture self-assembled to the targeted compounds during a low-temperature anneal. Resistivity measurements show that the number of PbSe layers per repeat unit (m) does not change the charge density transition onset temperature as previously reported for the analogous $[(SnSe)_{1+\delta}]_m(VSe_2)_1$ compounds. The temperature dependence and absolute values of the resistivity of the m = 3 and 4 heterostructures scale as expected for composite behavior. The difference in the thickness dependence of the CDW transition between the PbSe- and SnSe-containing compounds highlights that the identity of the intervening rock salt layer plays a more important role in modifying the CDW onset temperature than the separation of the VSe_2 layers.

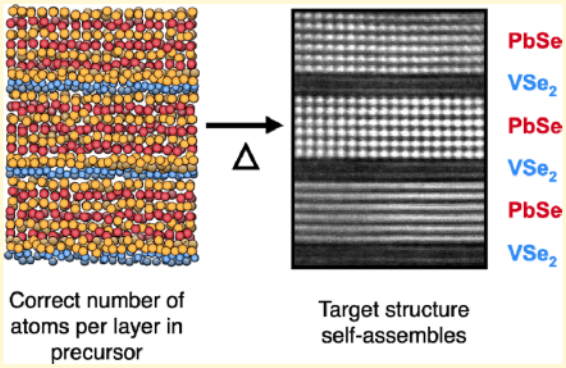

INTRODUCTION

The discovery of emergent properties in a single layer and very thin layers of quasi-two-dimensional systems has resulted in many reports of new systems and heterostructures.[1] Initially, the majority of the systems being investigated were semiconducting because large changes in properties were discovered in semiconducting systems and because single sheets of metallic systems were found to be unstable in air.[2] More recently, a number of interesting properties of metallic system have been explored as a function of thickness including superconductivity and charge density waves (CDWs).[3−5] The trends with layer thickness and/or layer separation depend on the specific property and compounds being investigated. The onset temperature of superconductivity is lowered when the thickness of $NbSe_2$ layers is reduced[6] or the separation between $NbSe_2$ layers in a heterostructure is increased.[7] Varying the layer thickness of different dichalcogenides produced opposite effects on the onset temperature of CDW transitions. Studies on mechanically exfoliated $TiSe_2$ have shown that as the thickness of the exfoliated $TiSe_2$ is decreased, the onset temperature of the CDW increased.[8] The opposite has been found for $TaSe_2$, with the onset temperature of the CDW decreasing as the thickness of the mechanically exfoliated film is decreased.[9] Unraveling the relationships between physical properties and the interaction between constituents at interfaces, the structure of the constituents and/or the electronic or magnetic properties of the constituents is a focus of continued interest.

The electrical and magnetic properties of vanadium dichalcogenides have been extensively investigated both computationally and experimentally, with a variety of contradictory results presented as the number of layers of VSe_2 is reduced. Bulk VSe_2 has vanadium in octahedral coordination in a 1T structure and is metallic. It also has a small Pauli

Received: July 16, 2019
Revised: September 25, 2019
Published: September 26, 2019

DOI: 10.1021/acs.chemmater.9b02826
Chem. Mater. 2019, 31, 8473−8483

paramagnetism because of the conduction electrons and exhibits a CDW transition. Density functional theory calculations predict the ground state of undistorted VSe_2 layers to be the ferromagnetic 2H-polytype with a metal to semimetal/semiconductor transition when going from the bilayer to the monolayer.[10−12] There are contradictory reports on how the CDW changes as the number of VSe_2 layers is reduced in this n-type metal and how magnetic behavior changes as the sample is thinned to a monolayer. The onset of the CDW in bulk single crystals of VSe_2 is 100 K[13] and it has been reported that this increases to 135 K as the thickness is reduced to 4−8 trilayers of VSe_2 prepared via liquid exfoliation.[14] An opposite trend was reported for micromechanically exfoliated nanoflakes, where the onset temperature decreases to 81 K at the lowest thickness measured, 11.6 nm.[5] The thin nanoflakes are n-type conductors, as is bulk VSe_2, but the carrier concentration increases as the nanoflake thickness is decreased. Both solvent-aided and mechanical exfoliation techniques were not able to precisely control the thickness of the VSe_2 flakes or reach the monolayer limit.[14,15]

Monolayer VSe_2 has been reported to have a CDW with a different distortion than found in the bulk.[16−18] The transition temperature is higher in the monolayer, and the transition temperature depends on both the material below it and the relative orientation of the adjacent layer. Monolayers of VSe_2 have also been reported to be ferromagnetic.[19] Other reports present data showing that their VSe_2 monolayers are nonmagnetic and suggest that the ferromagnetism results from oxide impurities.[20] Studies of $[(SnSe)_{1+\delta}]_m(VSe_2)_1$ and $[(PbSe)_{1+\delta}]_1(VSe_2)_1$ prepared by annealing designed precursors show that they are p-type metals with a CDW that depends on the thickness of the rock salt constituent.[21,22] The changes in electrical resistivity and charge carrier concentration at the CDW transition temperature are much larger than that observed in bulk VSe_2. Compounds with thicker VSe_2 layers, $[(SnSe)_{1+\delta}]_1(VSe_2)_n$ and $[(PbSe)_{1+\delta}]_1(VSe_2)_n$ where n is larger than two, are n-type metals and CDW transition and transition temperature are similar to those found in bulk VSe_2.[22,23]

In this paper, we probe the effect of changing the PbSe layer thickness on the CDW found in $[(PbSe)_{1+\delta}]_1(VSe_2)_1$. The synthesis, structure, and electrical properties of a family of new, metastable compounds, $[(PbSe)_{1+\delta}]_m(VSe_2)_1$, are discussed.[22] The synthesis of $[(PbSe)_{1+\delta}]_m(VSe_2)_1$ with m = 2, 3, and 4 was more challenging than the synthesis of the m = 1 compound because the higher m compounds have smaller barriers toward disproportionation into PbSe and VSe_2. Deviations in the composition of the precursor from the stoichiometry of the desired products result in disproportionation of the precursor during low-temperature annealing. The structure of the PbSe layers in $[(PbSe)_{1+\delta}]_m(VSe_2)_1$ compounds is significantly less distorted than found in the analogous semiconducting $[(PbSe)_{0.99}]_m(WSe_2)_n$[24] and $[(PbSe)_{1.00}]_m(MoSe_2)_n$[25] compounds. The electrical resistivity data of all of the $[(PbSe)_{1+\delta}]_m(VSe_2)_1$ compounds contain a CDW transition at ∼100 K that is distinctly different than that found in bulk VSe_2. The electrical resistivity can be successfully modeled using a parallel resistor circuit when m is 3 or greater, indicating composite behavior. These findings are very different from that previously reported for the isoelectronic $[(SnSe)_{1+\delta}]_m(VSe_2)_1$ compounds, where the CDW transition temperature changes systematically with m.[21] This suggests that the interaction between the constituent layers is more important than the separation of VSe_2 layers in determining the CDW transition temperature. The differences between these two sets of isoelectronic compounds demonstrate the sensitivity of emergent properties in heterostructures to the identity of the constituent layers.

EXPERIMENTAL SECTION

Precursors designed to form the compounds $[(PbSe)_{1+\delta}]_m(VSe_2)_1$ where $1 \leq m \leq 4$ were synthesized using the modulated elemental reactants (MER) technique. Pb (99.8% Alfa Aesar), V (99.995% Alfa Aesar), and Se (99.99% Alfa Aesar) were deposited using 6 kW electron beam guns (Pb and V) and a custom-made Knudsen effusion cell (Se) under high vacuum ($<3 \times 10^{-7}$ Torr). The precursors were prepared by sequentially evaporating elemental sources in the sequence [PbISe]$_m$VISe onto Si wafers or quartz substrates. The mass of each element deposited was monitored using quartz crystal monitors. A LabVIEW-based program opened and closed pneumatic shutters that control the amount of material deposited using either the integrated thickness or the product of the deposition rate and time. A more detailed explanation of the chamber and the deposition procedure is described by Fister, et al.[26] The amount of each element deposited in each sample was measured using X-ray fluorescence (XRF) on a Rigaku Primus II ZSX spectrometer. The proportionality factor between the measured fluorescence intensity and the number of atoms per unit area of each element in the film was determined as described by Hamann, et al.[27] The deposition conditions were iteratively adjusted to obtain precursors with the desired amounts of each element.

The layered precursors were crystallized by annealing in an inert N_2 atmosphere with an O_2 concentration less than 1 ppm. Out-of-plane specular X-ray diffraction (XRD), X-ray reflectivity (XRR), and X-ray rocking curve data were performed on a Bruker D8 Discover diffractometer with Cu Kα radiation (λ = 0.15418 nm). Grazing incidence in-plane XRD (GIXRD) scans were performed on a Rigaku SmartLab diffractometer. Le Bail fitting of the diffraction patterns was used to determine the in-plane lattice parameters using FullProf and GSAS software.[28,29] Rietveld refinement of the specular XRD patterns was done to determine the position of the atomic planes along the c-axis also using GSAS software.[29,30] High-angle annular dark-field scanning transmission electron microscopy (HAADF-STEM) images were collected by a FEI Titan G2 80-200 STEM with a Cs probe corrector, operated at 200 kV, using an annular detector with a collection range of 60−160 mrad. STEM samples were prepared by focused ion beam technique.

Resistivity and Hall coefficients were measured as a function of temperature on a film deposited on a quartz substrate using the van der Pauw technique. Data were collected at a temperature range between 25 and 295 K. Seebeck coefficients were measured using a custom measurement system in which Cu and constantan thermocouples were used to measure temperature and the voltage created by a small temperature difference in a film.

RESULTS AND DISCUSSION

The MER precursors were designed to have the correct composition and nanoarchitecture necessary to crystallize the target compounds. The number of atoms per square angstrom necessary to form the individual building blocks (PbSe and VSe_2) was calculated from the in-plane lattice parameters of the bulk structures of PbSe[31] and VSe_2[32] by dividing the number of atoms per unit cell by the basal plan area. The solid lines in Figure 1 give the calculated number of atoms of each element per unit area per repeating unit of the precursor for each targeted compound. The target number of V atoms per unit area per repeating sequence is constant as there is one VSe_2 trilayer in each repeat unit, whereas the number of atoms per unit area of Pb and Se increases linearly as the number of PbSe bilayer units (m) is increased. To prepare each of the compounds, m PbISe layers and a single VISe layer were

DOI: 10.1021/acs.chemmater.9b02826
Chem. Mater. 2019, 31, 8473−8483

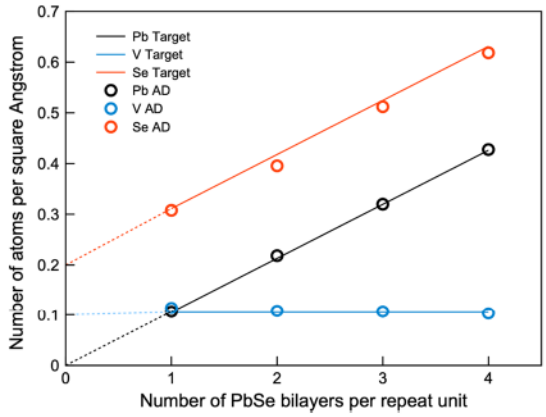

Figure 1. Calculated numbers of atoms per square angstrom for V, Pb, and Se based on bulk lattice parameters are shown as solid lines. The measured amounts of each element in the precursors are shown as filled circles. The deviations from the calculated number reflect the experimental challenges of controlling the deposition process to fractions of a monolayer. AD: as-deposited precursor.

sequentially deposited. For example, the precursor for $[(PbSe)_{1+\delta}]_2(VSe_2)_1$ was made by repeatedly depositing the following sequence of elemental layers: V|Se|Pb|Se|Pb|Se. The amount or each element in the Pb|Se and V|Se bilayers was iteratively adjusted to obtain the desired number of atoms per unit area to make a single unit cell thick layer of PbSe and VSe_2, respectively. The number of atoms/Å^2 per repeating unit for each element in the precursors was measured using XRF.[27] There is good agreement between the experimental and targeted number of atoms/Å^2 of each element in each precursor (Figure 1).

The nanoarchitecture of the precursors was measured using XRR and the data are presented in Figure 2. The XRR scans of each of the precursors contain Bragg reflections from the artificial layering of the elements and weaker subsidiary maxima from the finite thickness of the film. The first-order Bragg reflections shift to lower angles as the number of Pb|Se building blocks increases because of the increased thickness of the repeating structure. Precursor modulation lengths (λ) calculated from the first-order reflection linearly increase with the number of Pb|Se building blocks in the precursor (Figure 2 inset) and the measured thicknesses are all reasonable for the targeted heterostructures. The presence of the subsidiary maxima (Kiessig fringes[33]) to greater than 5° 2θ indicates that the films are smooth, with roughness calculated using the formula derived by Parratt of less than 6−8 Å across the analytical area.[34] The combination of the XRF and XRR data indicates that each precursor has close to the targeted amount of each element per unit area and the desired nanoarchitecture to form the targeted $[(PbSe)_{1+\delta}]_m(VSe_2)_1$ heterostructures.

The optimum annealing conditions to self-assemble the target heterostructures from the precursors were determined by an annealing study of the precursor with a 4(Pb|Se) + (V|Se) repeating sequence. The sample was annealed at a sequence of increasing temperatures for 1 h in an inert atmosphere and changes in structure were followed by collecting specular and in-plane XRD scans after each annealing temperature. Specular XRD scans (Figure 3) were used to track changes in long-range order in the c-axis direction in the film. The as-deposited diffraction pattern contains low angle reflections from the artificial modulation of the deposited elemental layers and broad high-order reflections (20°−40°

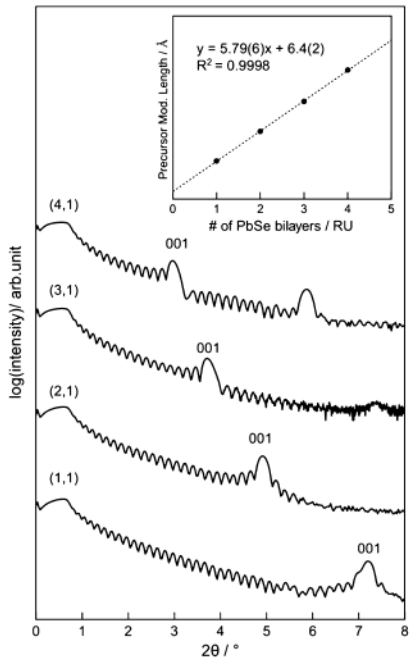

Figure 2. XRR patterns of the precursors designed to form the targeted $[(PbSe)_{1+\delta}]_m(VSe_2)_1$ compounds. The modulation length of the $(Pb|Se)_m$V|Se layer sequence determined from the position of the first-order Bragg reflection is graphed vs the number of Pb|Se layers (m) in the repeating layer sequence in the inset.

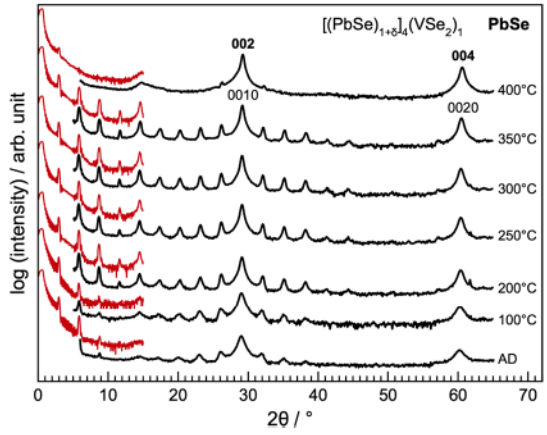

Figure 3. XRR and specular XRD patterns collected as a function of increasing temperature after annealing a 4(Pb|Se)(V|Se) precursor at the indicated temperatures for 1 h.

2θ), indicating that the film has begun to self-assemble with a period consistent with the targeted heterostructure. The reflections from both phenomena can be indexed as 00l reflections. The period of the low angle reflections (30.21(1) Å) is reasonably close to that expected from the repeating structure deposited. The c-axis lattice parameter of the developing heterostructure is slightly larger, 30.67(3) Å. The higher angle reflections become narrower and more intense after the sample is annealed at 200 °C, indicating the start of crystal growth of one or both constituent layers at this temperature, resulting in a more coherent structure. After the 250, 300, and 350 °C annealing periods, the intensity of the reflections increase, indicating continued crystal growth. There are only small changes in the peak locations, however, indicating a near constant c-axis lattice parameter. The low

DOI: 10.1021/acs.chemmater.9b02826
Chem. Mater. 2019, 31, 8473−8483

angle reflections become broader and shift to a higher angle as annealing temperature is increased, becoming consistent in line width and *c*-axis lattice parameter with the higher angle reflections of the heterostructures after the 300 °C anneal. The Laue reflections from the finite number of unit cells in the film also increase in intensity, indicating that a coherent structure is forming with a uniform number of unit cells across the analytical area. After the 400 °C annealing, the superlattice reflections are almost completely absent, suggesting that the heterostructure has decomposed. The two intense reflections remaining can be indexed as 002 and 004 reflections of PbSe. The broad reflection at ∼14° 2θ is consistent with the 001 reflection of small VSe_2 crystallites. This suggests that at 400 °C, there is enough energy to make the heterostructures disproportionate into a mixture of binary constituents. The targeted heterostructures with thicker PbSe layers are less thermally stable than $[(PbSe)_{1+\delta}]_1(VSe_2)_1$, which was reported to be stable at 400 °C.[35]

In-plane diffraction patterns were collected during the annealing study to follow the evolution of the in-plane structure of the films and are shown in Figure 4. In the as-deposited precursor, broad reflections are present that can be indexed as *hk*0 reflections of a hexagonal and a square lattice. The reflections shift to slightly higher angles after the sample is annealed at 100 °C. The lattice parameters of the hexagonal (a = 3.393(4) Å) and square lattices (a = 6.0891(2) Å) above 100 °C are close to the lattice parameters of bulk VSe_2[32] and PbSe.[31] There is a significant increase in the intensity of the 110 VSe_2 peak after annealing at 200 °C, suggesting that significant crystal growth of VSe_2 occurs at this temperature. Intensities of both the VSe_2 and PbSe reflections continue to increase as the annealing temperature is increased up to 350 °C. Weak reflections are present with odd indices for the square constituent. The reflections are consistent with the condition that $h + k = 2n$, indicating that the PbSe bilayer is distorted from the bulk face-centered cubic structure. Both constituents are still present at 400 °C, although the intensity of all reflections are lower and the reflections with odd indices in the square lattice are no longer detectable. This suggests that the loss of the heterostructure reflections in the specular diffraction data after annealing at 400 °C results from disproportionation of the heterostructure into PbSe and VSe_2 regions. The broad 001 reflections for VSe_2 in the specular scan indicate that large crystallographically aligned domains of VSe_2 do not form. The specular and in-plane diffraction data collected as a function of annealing temperature suggest that optimal processing conditions to convert the 4(PbISe)(VISe) precursor into $[(PbSe)_{1+\delta}]_4(VSe_2)_1$ is 300 °C for 1 h.

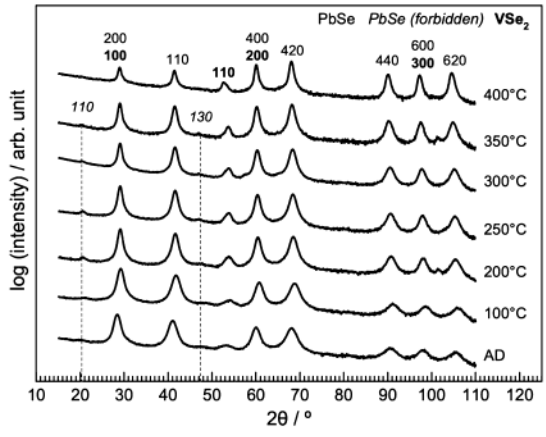

Figure 4. In-plane XRD patterns collected as a function of increasing temperature after annealing a (VISe) + 4(PbISe) precursor at the indicated temperatures for 1 h.

The absolute amounts of each element in each layer were found to be very important in controlling whether the targeted compounds self-assembled. The low temperature of the substrate during the deposition limits surface diffusion rates, so atoms cannot move far before being buried by the incoming flux of atoms. The diffraction data in the annealing study indicate that both PbSe and VSe_2 nucleate and grow during the deposition. If the amount of each bilayer (PbISe or VISe) deposited corresponds to a complete single structural unit and nucleation occurs during the deposition, then the precursor layers develop a significant long-range order during the deposition (Figure 5, scheme II). If the amount of a deposited element deviates from the targeted value, then the extra (or missing) atoms result in partial layers. This increases the roughness in the layers and causes nucleation of the binary structures at different heights relative to the substrate. Annealing the sample at elevated temperatures activates diffusion, enabling atoms to move around to lower the free energy by eliminating defects and optimizing local coordination geometries. As a result, off-composition samples form partial layers in addition to interstitials and/or vacancies in the heterostructures (Figure 5, scheme III). If the number of atoms in each layer deviates significantly from that required for an integer number of layers, then disproportionation occurs during annealing (Figure 5, scheme I). The ability to determine the number of atoms of each element per repeating

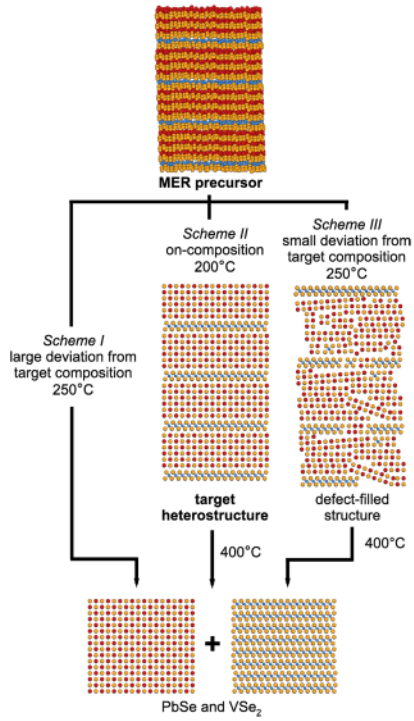

Figure 5. Proposed reaction pathway for the formation of products from a 3(PbISe) + 1(VISe) precursor. The pathway depends on the absolute number of atoms per repeat unit of the precursor. The thermodynamic product is a disproportionation of the precursor into isolated regions of PbSe and VSe_2.

DOI: 10.1021/acs.chemmater.9b02826
Chem. Mater. 2019, 31, 8473−8483

layer in the precursor using XRF is a critical advance, as it speeds up optimization of the deposition process and also enables us to predict which precursors are likely to form the targeted compounds.

Our assumption in this study is that precursors with the correct composition and nanoarchitecture, when annealed in the right conditions, should assemble to the target structure. We annealed the four precursors whose data are contained in Figures 1 and 2 using the optimized processing parameters and the specular diffraction patterns of the resulting compounds are shown in Figure 6. All the peaks in the diffraction patterns

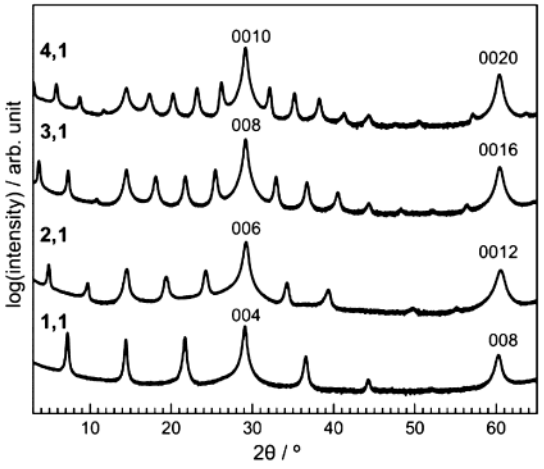

Figure 6. Specular XRD patterns of $[(PbSe)_{1+\delta}]_m(VSe_2)_1$ (m = 1, 2, 3, 4) heterostructures.

can be indexed as 00l reflections, consistent with heterostructures forming with their c axis perpendicular to the substrate. The c-axis lattice parameters of the annealed sample have a linear relationship with the number of PbSe bilayers in each repeat unit, which is consistent with the modulation length of the precursors being preserved as they crystallize. The average change in c-axis lattice parameter per PbSe bilayer added (6.12(1) Å) is within an error of the c-lattice parameter of bulk rock salt PbSe (6.1213(8) Å)[31] and equivalent PbSe bilayer thicknesses found in other heterostructures ($[(PbSe)_{1+\delta}]_m(NbSe_2)_1$) (6.12) and ($[(PbSe)_{1+\delta}]_1(TiSe_2)_n$), (6.13(6) Å).[36,37] PbSe bilayer thicknesses in $[(PbSe)_{1+\delta}]_1(NbSe_2)_n$ and $[(PbSe)_{1+\delta}]_m(MoSe_2)_n$ are slightly greater than found in this work.[7,38] As there is only one VSe_2 in each repeat unit, the y-intercept of a graph of the c-axis lattice parameter versus the number of PbSe bilayers (Figure S1) is greater than observed in bulk VSe_2, as the intercept is the sum of the average thickness of each VSe_2 trilayer and the thickness of the van der Waals gap. The PbSe and VSe_2 thicknesses obtained from this graph are close to their respective bulk equivalents and previous work on PbSe- and VSe_2-containing heterostructures. The c-axis lattice parameters of the PbSe-containing heterostructures are very close to those reported previously for analogous SnSe-containing heterostructures (Figure S1), and the change in inter-VSe_2 distances as m increases is within the experimental error.

The low-angle XRR patterns (Figure 7) contain Kiessig fringes/Laue reflections between Bragg reflections extending to high angles, indicating that the films consist of a consistent number of unit cells over the analytical volume. The films become smoother after annealing, with roughness decreasing

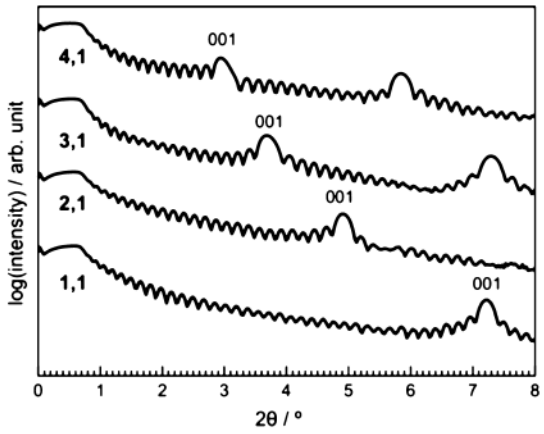

Figure 7. Low-angle XRR patterns of $[(PbSe)_{1+\delta}]_m(VSe_2)_1$ (m = 1, 2, 3, 4) heterostructures.

to 4−6 Å, as evidenced by the increase in the number of observed Kiessig fringes. Indexing the low-angle Kiessig fringes and using a modified version of Bragg's law corrected for refraction enabled us to calculate the total film thicknesses. Each film has a total thickness of approximately 50 nm, consistent with the targeted thicknesses. Dividing the total film thickness by the calculated c-axis lattice parameter of the heterostructures yields the integral number of unit cells in the films. The numbers of repeat units formed calculated from the number of Kiessig fringes between Bragg peaks (Table 1) and

Table 1. Structural Parameters Calculated from the XRR and Specular XRD Patterns

m,n	c-axis lattice parameter (Å)	total film thickness (Å)	# of layers	targeted # of layers
1,1	12.273(4)	481.3(3)	39	41
2,1	18.343(8)	492.5(2)	27	27
3,1	24.486(9)	491.8(3)	20	20
4,1	30.617(9)	493.3(4)	16	16

the number of repeat units deposited are equal to one another, except in the m = 1 sample, where the number of unit cells formed is two less than the number of deposited layers. XRF data show that there is an increase in oxygen in this film after annealing, suggesting that the two layers might have been lost to oxidation at the top of the film. The specular diffraction data indicate that each PbISe and VISe bilayer in the deposited precursors crystallizes a PbSe bilayer or VSe_2 layer in the targeted structures.

The in-plane diffraction patterns of the $[(PbSe)_{1+\delta}]_m(VSe_2)_1$ (m = 1, 2, 3, 4) heterostructures are shown in Figure 8. All of the reflections can be indexed as hk0 reflections of a hexagonal and a square in-plane unit cell, consistent with the formation of VSe_2 and PbSe layers in the heterostructures (Table 2). This indicates that the film has a preferred alignment with the c-axis perpendicular to the substrate, consistent with the specular diffraction data. The hexagonal basal plane unit cell with a lattice parameter of 3.40−3.43 Å is consistent with that reported for VSe_2.[32] The square basal plane unit cell is smaller for the m = 1 compound (6.03 Å) than for the m = 2−4 compounds (6.11−6.13 Å), but all are close to that reported for PbSe.[31] However, the hk0 Bragg reflections where h and k are both odd, forbidden in an undistorted rock salt structure, are observed. The presence of 110 and 130 reflections

DOI: 10.1021/acs.chemmater.9b02826
Chem. Mater. 2019, 31, 8473−8483

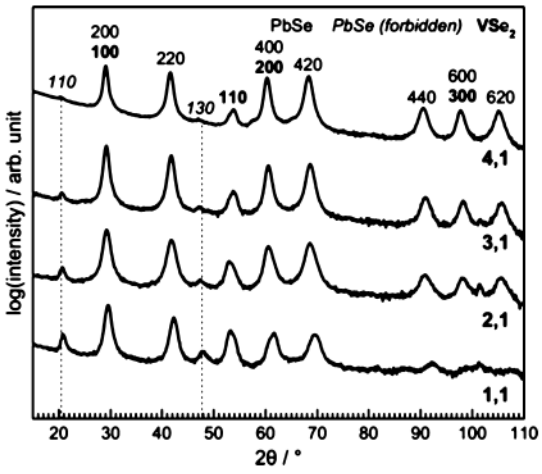

Figure 8. Grazing incidence in-plane XRD of self-assembled $[(PbSe)_{1+\delta}]_m(VSe_2)_1$ (m = 1, 2, 3, 4) heterostructures.

Table 2. In-Plane Lattice Parameters Derived from the Diffraction Patterns via Le Bail Fitting[a]

m,n	a-axis lattice parameter, VSe_2 (Å)	a-axis lattice parameter, PbSe (Å)	misfit parameter, δ
1,1	3.425(1)	6.030(1)	1.12
2,1	3.447(1)	6.116(1)	1.10
3,1	3.404(1)	6.106(5)	1.08
4,1	3.408(1)	6.130(1)	1.07

[a]Misfit lattice parameters were calculated using the lattice parameters and the stoichiometric coefficients of each constituent.

indicates that Pb and Se are not located at (0,0) and (1/2,1/2) respectively in the intergrowth. A possible distortion that may give rise to these forbidden reflections is a lateral translation of one of the PbSe layers relative to one another. The intensities of the forbidden reflections decrease as the thickness of the PbSe constituent is increased, indicating that the magnitude of the distortion decreases. Forbidden reflections have also been observed in the in-plane diffraction patterns of $[(PbSe)_{1.14}]_1(NbSe_2)_n$ heterostructures,[39] suggesting that a distortion is a common feature of PbSe bilayers flanked by dichalcogenides in ferecrystals.

HAADF-STEM was collected to show the bonding arrangement of the atoms in the film and the relationship between the PbSe and VSe_2 layers in the heterostructures. This information is not present in the specular and in-plane diffraction patterns because of the preferred alignment in the films. The HAADF-STEM image of a representative portion of the $[(PbSe)_{1+\delta}]_3(VSe_2)_1$ sample is shown in Figure 9a. Both constituents are clearly distinguishable from each other because the PbSe layers are significantly brighter than the VSe_2 layers. The microscopy data confirm that the film consists of alternating layers of PbSe (six planes or three bilayers) and one VSe_2 trilayer. Defects are clearly present, presumably because of different nucleation sites that grow together during the self-assembly process. The atoms in the VSe_2 layers, when viewed down the ⟨110⟩ zone axis, appear along a diagonal line, indicating that the V atoms are octahedrally coordinated, similar to the bulk binary compound.[40] The PbSe layers, observed down ⟨100⟩ and off-axis zones, both show that it has a structure similar to the rock salt structure found in the analogous $[(PbSe)_{1+\delta}]_m(WSe_2)_n$ heterostructure.[41] The integrated intensity profile across the slice of the image provides

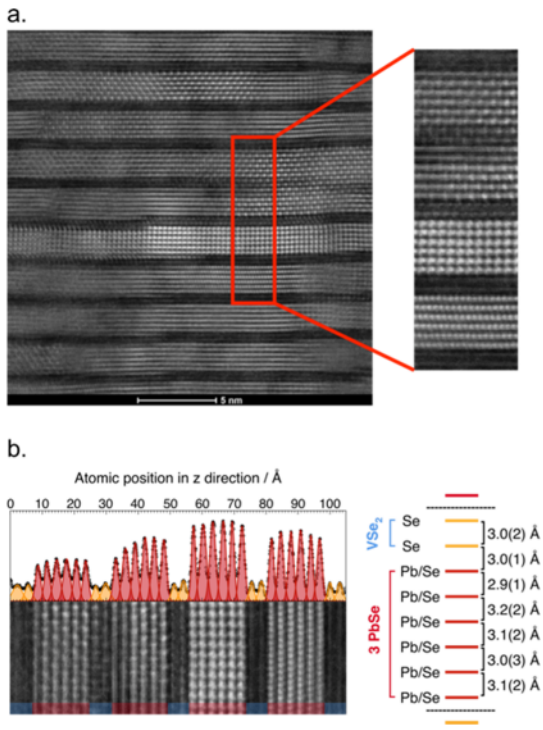

Figure 9. (a) HAADF-STEM image of the $[(PbSe)_{1+\delta}]_3(VSe_2)_1$ heterostructure showing that the film consists of PbSe (bright rows) and VSe_2 (dark rows); (b) Linear profile of a slice of the image showing approximate atomic plane positions in a repeat unit.

the positions of the atomic planes along the c-axis as shown in Figure 9b. The average atomic plane distances between Pb/Se planes, shown in the right of Figure 9b, are all within error of each other. This is different from what was observed in the analogous compound $[(PbSe)_{1+\delta}]_3(MoSe_2)_1$, where the PbSe planes had alternating short and long distances, indicating discrete bilayers.[42] The lack of this distortion in $[(PbSe)_{1+\delta}]_3(VSe_2)_1$ perhaps results from a change in the interaction between the PbSe and dichalcogenide layers because of the change in electronic properties of the dichalcogenide (trigonal prismatic $MoSe_2$ is semiconducting,[43] whereas octahedral VSe_2 is metallic[44]). The availability of available states in metallic VSe_2 will result in virtual states between PbSe and VSe_2 as found at metal−semiconductor interfaces.[45] The reduced distortion in the PbSe layer in $[(PbSe)_{1+\delta}]_3(VSe_2)_1$ relative to $[(PbSe)_{1+\delta}]_3(MoSe_2)_1$ indicates a weaker interaction, consistent with the reduced kinetic stability of $[(PbSe)_{1+\delta}]_3(VSe_2)_1$ relative to $[(PbSe)_{1+\delta}]_3(MoSe_2)_1$.[42] The distance between the metal plane in the dichalcogenide to the average position of Pb/Se distance in the V-compound is 10% smaller (4.5(1) Å) than in the Mo-compound (5.0 Å), reflecting both the different coordination in the dichalcogenide and the different interaction between PbSe and the different dichalcogenides. In Figure 9a, multiple zone axes for the PbSe layers are observed, indicating rotational disorder between the constituents.

Fractional z-axis coordinates obtained from the HAADF-STEM analysis of the $[(PbSe)_{1+\delta}]_3(VSe_2)_1$ heterostructure were used as an initial model for a Rietveld refinement of the specular diffraction data. The diffraction data, calculated diffraction intensities from the refined structural model and the difference between them are shown in Figure 10, along

DOI: 10.1021/acs.chemmater.9b02826
Chem. Mater. 2019, 31, 8473−8483

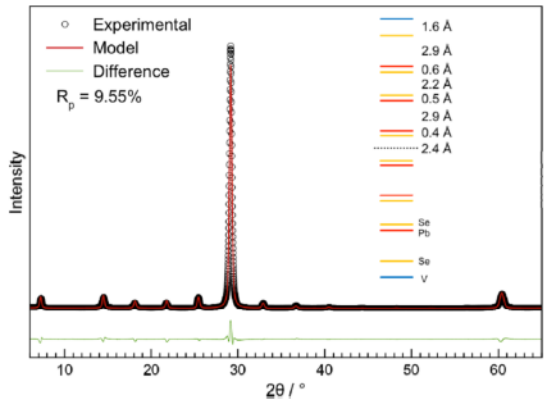

Figure 10. Results of a Rietveld refinement of the corresponding specular XRD of the heterostructure and a comparison of the structural model refined to the HAADF-STEM-derived atomic positions.

with the refined structural model. The consistency between the structure derived from the HAADF-STEM and Rietveld refinement of the XRD suggests that the majority of the film consists of the heterostructure. The Pb and Se planes are not coincident and there is an alternation of short and long distances between Pb (or Se) planes, consistent with the formation of PbSe bilayers. This distortion is smaller than that observed in $[(PbSe)_{1+\delta}]_3(MoSe_2)$.[42]

Resistivity, Hall coefficients, and Seebeck coefficients were measured to investigate the impact of the increased PbSe thickness and associated structural changes on electrical transport properties. As PbSe is semiconducting[46] and VSe_2 is metallic,[44] conduction in the compounds studied here is expected to take place primarily in the VSe_2 layers as previously reported for $[(PbSe)_{1+\delta}]_m(NbSe_2)_1$ and $[(PbSe)_{1+\delta}]_1(VSe_2)_n$ ferecrystals and misfit layer compounds containing metallic dichalcogenides.[22,36] The room temperature resistivity of $[(PbSe)_{1+\delta}]_1(VSe_2)_1$ is consistent with previously published values,[22] and the resistivity values systematically increase as m increases (Figure 11). The differences in the resistivity between samples with adjacent m values decrease as m increases. The increase in resistivity as m increases was expected as a larger fraction of the film consists of semiconducting PbSe as m increases. The room temperature

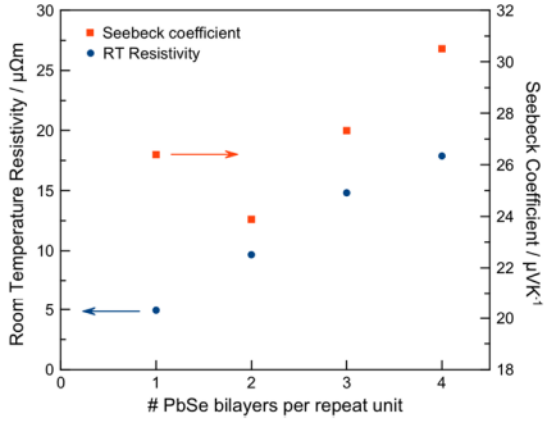

Figure 11. Room temperature Seebeck coefficients and resistivity graphed as a function of the number of PbSe bilayers in the respective compounds.

resistivity values for the $[(PbSe)_{1+\delta}]_m(VSe_2)_1$ compounds, however, are approximately twice as large as those reported for the analogous $[(SnSe)_{1+\delta}]_m(VSe_2)_1$ compounds.[21] We speculate that this is a consequence of the differences in the band gaps of SnSe and PbSe and a difference in the alignment of the VSe_2 bands with those of SnSe and PbSe. The room temperature Seebeck coefficients are positive and the magnitude is typical for metallic behavior. The Seebeck coefficients, however, do not systematically increase as m is increased, which would be expected from the decrease in carrier concentration. The larger than expected Seebeck coefficient for the $[(PbSe)_{1+\delta}]_1(VSe_2)_1$ compound suggests that transport in this compound is more complicated, perhaps because only a 0.6 nm bilayer of PbSe separates the VSe_2 layers. The wave function tails of VSe_2 within the PbSe layer overlap more in $[(PbSe)_{1+\delta}]_1(VSe_2)_1$ than in the compounds with thicker PbSe layers.

The resistivity and carrier concentrations calculated from Hall coefficients assuming a single band are graphed in Figure 12 as a function of temperature. The room temperature Hall coefficients are all positive and change systematically as m is increased, indicating that holes are the majority carrier and that a decrease in carrier concentration causes the increase in resistivity as m increases. The carrier concentrations calculated assuming a single band model are in the range expected for a metal, consistent with the data presented in Figure 11. The

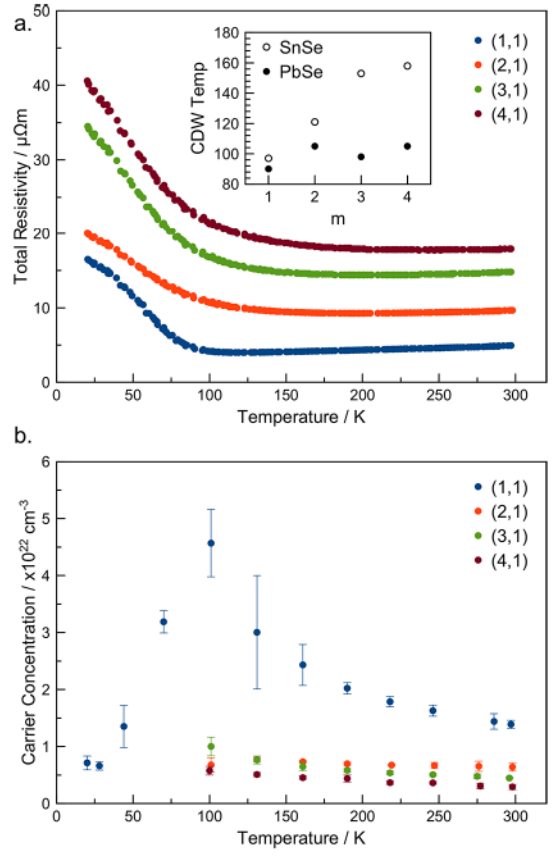

Figure 12. (a) Temperature dependence of resistivity and (b) carrier concentrations calculated from Hall coefficients assuming a single band model for $[(PbSe)_{1+\delta}]_m(VSe_2)_1$ (m = 1, 2, 3, 4) heterostructures. The inset of top plot shows a comparison of the CDW transition temperatures for $[(PbSe)_{1+\delta}]_m(VSe_2)_1$ and $[(SnSe)_{1+\delta}]_m(VSe_2)_1$ compounds.

DOI: 10.1021/acs.chemmater.9b02826
Chem. Mater. 2019, 31, 8473−8483

sign of the Hall coefficient is opposite to that reported for bulk VSe_2. The temperature dependences of the resistivity of the different $[(PbSe)_{1+\delta}]_m(VSe_2)_1$ compounds are all very similar. Between 150 and 300 K, the resistivity slowly decreases with decreasing temperature as expected for a metal. The rate of the decrease is 2−3 times smaller than that found in bulk VSe_2, suggesting a reduced electron−phonon scattering. Between 90 and 105 K, depending on the value of m, the resistivity rapidly increases to a value at about 20 K that is 2−3 times larger than the room temperature value. This substantial increase in the resistivity is different from what is found in bulk VSe_2 and similar to that reported for the analogous $[(SnSe)_{1+\delta}]_m(VSe_2)_1$ compounds, which was shown to be caused by a CDW transition.[21] The transition in $[(PbSe)_{1+\delta}]_1(VSe_2)_1$ is sharper than in the compounds with thicker PbSe layers and occurs at approximately 90 K. For the other three compounds, the transition is broader and the transition temperature occurs at a slightly higher temperature. The addition of PbSe bilayers to the $[(PbSe)_{1+\delta}]_1(VSe_2)_1$ does not systematically increase the CDW transition temperature (Figure 12a inset), as was observed in $[(SnSe)_{1+\delta}]_m(VSe_2)_1$ compounds.[21] The ∼10 K increase in the CDW onset temperature as m is increased is also significantly smaller than the increase observed for $[(SnSe)_{1+\delta}]_m(VSe_2)_1$ compounds.[21]

The temperature dependence of the carrier concentrations provides additional information, although we unfortunately were not able to measure the Hall coefficient for the higher m compounds below the CDW onset temperature. For the $m = 1$ compound, the carrier concentration has a strong temperature dependence, increasing as temperature is decreased from room temperature and then decreasing abruptly at the CDW onset. The temperature dependence suggests that a simple single band, free electron model is probably not appropriate for this compound. A similar temperature dependence was observed for $[(SnSe)_{1+\delta}]_1(VSe_2)_1$. The carrier concentrations of the samples with thicker PbSe layers increase slightly as temperature decreases. The carrier concentration decreases as m is increased as the semiconducting PbSe dilutes the carriers from the metallic VSe_2 layer.

A simple model for the electrical properties of the $[(PbSe)_{1+\delta}]_m(VSe_2)_1$ compounds is to consider the sample to be a composite consisting of noninteracting parallel conductors. If we assume that the resistivity of the PbSe layer is much higher than the resistivity of the VSe_2 layer, then it can be shown that

$$\rho_{VSe_2} = \rho_{exp}[n/(m+n)] \quad (1)$$

where ρ_{exp} is the measured resistivity, n is the number of VSe_2 layers in the repeating unit (one for this set of samples), and m is the number of PbSe bilayers.[36] If eq 1 is valid, then the resistivity obtained for a monolayer of VSe_2 from each compound will be the same. Equation 1 also describes the expected change in carrier concentration assuming composite behavior. Figure 13 graphs the temperature dependence of the resistivity and carrier concentration of a VSe_2 monolayer obtained from each compound using this equation. The calculated resistivity of the VSe_2 monolayer increases as m increases, with the $m = 3$ and 4 samples having very similar resistivity values. The calculated carrier concentration for a monolayer of VSe_2 from $[(PbSe)_{1+\delta}]_1(VSe_2)_1$ data is higher than those calculated from the higher m compounds. The carrier concentrations are very similar for the higher m compounds between 200 and 300 K. There is an increase in the carrier concentrations as the CDW transition temperature is approached. This suggests that the electrical properties can be described as that of a composite of a metallic VSe_2 monolayer separated by a nonconducting PbSe layer when m is 3 or greater. Though composite behavior is observed with higher values of m, the electrical transport properties of $[(PbSe)_{1+\delta}]_m(VSe_2)_1$ are still distinctly different from their bulk constituents. The CDW wave of the heterostructures is also distinctly different from bulk VSe_2, with holes being the majority carrier and markedly different temperature dependences of resistivity and Hall coefficients, suggesting a distinctly different CDW in the VSe_2 monolayers.

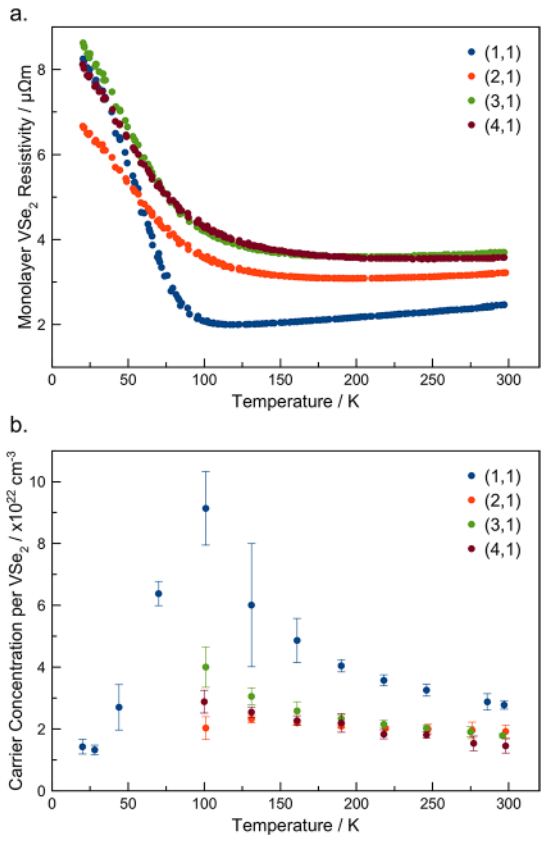

Figure 13. Calculated (a) resistivity and (b) carrier concentrations for a monolayer of VSe_2 using eq 1 and the data in Figure 11. If eq 1 is valid, the resistivity and carrier concentration calculated from each of the compounds should be the same.

As the wave function of the metallic VSe_2 monolayer will extend into the semiconducting PbSe, which acts as a dielectric,[45] this composite behavior suggests that when m is 3 the distance between adjacent VSe_2 monolayers is large enough that the wavefunction tails in adjacent layers do not significantly overlap. The lower resistivity observed for the VSe_2 monolayer in $[(PbSe)_{1+\delta}]_1(VSe_2)_1$ would then result from the overlap of the wave function tails of adjacent VSe_2 monolayers, as the bilayer of PbSe that separates them is only 0.6 nm thick.

It is interesting to compare the electrical properties of the $[(PbSe)_{1+\delta}]_m(VSe_2)_1$ compounds presented here with those reported previously for $[(SnSe)_{1+\delta}]_m(VSe_2)_1$ compounds[21] and members of both families with thicker VSe_2 layers. In both sets of compounds, the electrical data indicate that VSe_2 monolayers are metallic and have a distinctly different CDW

DOI: 10.1021/acs.chemmater.9b02826
Chem. Mater. 2019, 31, 8473−8483

than that found in thicker VSe_2 layers. Both compounds with $m = n = 1$ have similar changes in the carrier concentration calculated from the Hall coefficient assuming a single band model, increasing significantly as temperature is decreased and then dropping precipitously at the CDW onset temperature. $[(PbSe)_{1+\delta}]_m(VSe_2)_1$ compounds with $m = 3$ and 4 have composite behavior, however, whereas the analogous $[(SnSe)_{1+\delta}]_m(VSe_2)_1$ compounds[21] do not. This is perhaps related to the structural changes in the MSe layers as a function of thickness. In both PbSe and SnSe, there are two distortions that occur from a rock salt structure; a puckering distortion of the layers where the metal atoms are above and the Se atoms below the average plane, and an alternating long and short interlayer distance between MSe bilayers. Both of these distortions change systematically as m is increased. In the $[(SnSe)_{1+\delta}]_m(VSe_2)_1$ compounds,[21] the puckering distortion increases as m increases as the SnSe. In $[(PbSe)_{1+\delta}]_m(VSe_2)_1$ compounds, however, both the puckering distortion and the difference between the inter- and intra-bilayers decrease as m increases. This difference in behavior is related to the different structures of SnSe and PbSe. SnSe has an orthorhombic structure at room temperature that becomes cubic as temperature is raised.[47] A single bilayer of SnSe has a structure close to the cubic high temperature structure, and the structure approaches the bulk low temperature structure as layer thickness is increased.[48] As many as 30 bilayers of SnSe are required to obtain lattice parameters that are consistent with the bulk structure.[49] PbSe, however, has a simple rock salt structure. A single bilayer of PbSe distorts from the rock salt structure and the distortion decreases as m increases and approaches the bulk structure when m is typically around 5 or 6.[42] In the $[(PbSe)_{1+\delta}]_m(VSe_2)_1$ series, however, the structure seems to be approaching the bulk quicker. The transition from a new material, with properties distinct from the constituent layers, to a composite of VSe_2 monolayers separated by a PbSe nonconducting layer occurs at 3−4 PbSe bilayers based on electrical properties.

CONCLUSIONS

In this work, we showed that the compounds $[(PbSe)_{1+\delta}]_m(VSe_2)_1$ with m from 1 to 4 could be prepared from designed precursors. The correct local number of atoms per unit area per repeating unit and the correct nanoarchitecture were necessary for the precursor to self-assemble into the targeted metastable products during low temperature annealing. The compounds with larger m values are less kinetically stable than $[(PbSe)_{1+\delta}]_1(VSe_2)_1$ and the precursors need to be closer to the targeted number of atoms per unit area. Diffraction data and HAADF-STEM images indicate that PbSe in the heterostructures has a lower symmetry structure than face centered cubic, presumably because of the interface and interlayer interactions. All of the $[(PbSe)_{1+\delta}]_m(VSe_2)_1$ compounds have an abrupt increase in resistivity as temperature is decreased, which is consistent with a CDW. The onset temperature of the CDW transition does not change significantly as m is increased. The transport behavior for the $m = 3$ and 4 compounds can be described using a composite model consisting of a conducting monolayer of VSe_2 and a nonconducting PbSe layer that do not interact. The difference in the rock salt layer thickness dependence of the CDW transition temperature between members of $[(PbSe)_{1+\delta}]_m(VSe_2)_1$ and $[(SnSe)_{1+\delta}]_m(VSe_2)_1$, which have approximately the same VSe_2 interlayer distance, suggests that the identity of the intervening constituent and its interaction with the VSe_2 monolayer determine the CDW onset temperature.

ASSOCIATED CONTENT

Supporting Information

The Supporting Information is available free of charge on the ACS Publications website at DOI: 10.1021/acs.chemmater.9b02826.

Comparison of the c-lattice parameters of the PbSe- and SnSe-containing heterostructures and Rietveld refinement results (PDF)

AUTHOR INFORMATION

Corresponding Author

*E-mail: davej@uoregon.edu.

ORCID

Dmitri Leo Mesoza Cordova: 0000-0002-7527-8950

David C. Johnson: 0000-0002-1118-0997

Author Contributions

The paper was written through contributions of all authors.

Funding

National Science Foundation grant DMR-1710214.

Notes

The authors declare no competing financial interest.

ACKNOWLEDGMENTS

The authors acknowledge support from the National Science Foundation under grant DMR-1710214. We also acknowledge the Center for Advanced Materials Characterization in Oregon (CAMCOR) at the University of Oregon. This work was performed, in part, at the Center for Integrated Nanotechnologies, an Office of Science User Facility operated for the U.S. Department of Energy (DOE) Office of Science by Los Alamos National Laboratory (Contract DE-AC52-06NA25396) and Sandia National Laboratories (Contract DE-NA-0003525).

ABBREVIATIONS

CDW, charge density wave; XRF, X-ray fluorescence; XRD, X-ray diffraction; XRR, X-ray reflectivity; GIXRD, grazing incidence in-plane X-ray diffraction; HAADF STEM, high-angle annular dark-field scanning transmission electron microscopy

REFERENCES

(1) Hamann, D. M.; Hadland, E. C.; Johnson, D. C. Heterostructures Containing Dichalcogenides-New Materials with Predictable Nanoarchitectures and Novel Emergent Properties. *Semicond. Sci. Technol.* **2017**, *32*, 093004.

(2) Geim, A. K.; Grigorieva, I. V. Van Der Waals Heterostructures. *Nature* **2013**, *499*, 419−425.

(3) Wang, H.; Huang, X.; Lin, J.; Cui, J.; Chen, Y.; Zhu, C.; Lui, F.; Zeng, Q.; Zhou, J.; Yu, P.; et al. High-Quality Monolayer Superconductor $NbSe_2$ Grown by Chemical Vapour Deposition. *Nat. Commun.* **2017**, *8*, 394.

(4) Tsen, A. W.; Hovden, R.; Wang, D.; Kim, Y. D.; Okamoto, J.; Spoth, K. A.; Liu, Y.; Lu, W.; Sun, Y.; Hone, J. C.; et al. Structure and Control of Charge Density Waves in Two-Dimensional 1T-TaS_2. *Proc. Natl. Acad. Sci. U.S.A.* **2015**, *112*, 15054−15059.

(5) Yang, J.; Wang, W.; Liu, Y.; Du, H.; Ning, W.; Zheng, G.; Jin, C.; Han, Y.; Wang, N.; Yang, Z.; et al. Thickness Dependence of the

DOI: 10.1021/acs.chemmater.9b02826
Chem. Mater. 2019, 31, 8473−8483

Charge-Density-Wave Transition Temperature in VSe_2. *Appl. Phys. Lett.* **2014**, *105*, 063109.
(6) Xi, X.; Zhao, L.; Wang, Z.; Berger, H.; Forró, L.; Shan, J.; Mak, K. F. Strongly Enhanced Charge-Density-Wave Order in Monolayer $NbSe_2$. *Nat. Nanotechnol.* **2015**, *10*, 765−769.
(7) Grosse, C.; Alemayehu, M. B.; Falmbigl, M.; Mogilatenko, A.; Chiatti, O.; Johnson, D. C.; Fischer, S. F. Superconducting Ferecrystals: Turbostratically Disordered Atomic-Scale Layered $(PbSe)_{1.14}(NbSe_2)_n$ Thin Films. *Sci. Rep.* **2016**, *6*, 33457.
(8) Goli, P.; Khan, J.; Wickramaratne, D.; Lake, R. K.; Balandin, A. A. Charge Density Waves in Exfoliated Films of van der Waals Materials: Evolution of Raman Spectrum in $TiSe_2$. *Nano Lett.* **2012**, *12*, 5941−5945.
(9) Yan, Z.; Jiang, C.; Pope, T. R.; Tsang, C. F.; Stickney, J. L.; Goli, P.; Renteria, J.; Salguero, T. T.; Balandin, A. A. Phonon and thermal properties of exfoliated $TaSe_2$ thin films. *J. Appl. Phys.* **2013**, *114*, 204301.
(10) Li, F.; Tu, K.; Chen, Z. Versatile Electronic Properties of VSe_2 Bulk, Few-Layers, Monolayer, Nanoribbons, and Nanotubes: A Computational Exploration. *J. Phys. Chem. C* **2014**, *118*, 21264−21274.
(11) Abdul Wasey, A. H. M.; Chakrabarty, S.; Das, G. P. Quantum size effects in layered VX_2 (X = S, Se) materials: Manifestation of metal to semimetal or semiconductor transition. *J. Appl. Phys.* **2015**, *117*, 064313.
(12) Lebègue, S.; Björkman, T.; Klintenberg, M.; Nieminen, R. M.; Eriksson, O. Two-Dimensional Materials from Data Filtering and *Ab Initio* Calculations. *Phys. Rev. X* **2013**, *3*, 031002.
(13) Thompson, A. H.; Silbernagel, B. G. Correlated magnetic and transport properties in the charge-density-wave states of VSe_2. *Phys. Rev. B: Condens. Matter Mater. Phys.* **1979**, *19*, 3420−3426.
(14) Xu, K.; Chen, P.; Li, X.; Wu, C.; Guo, Y.; Zhao, J.; Wu, X.; Xie, Y. Ultrathin Nanosheets of Vanadium Diselenide: A Metallic Two-Dimensional Material with Ferromagnetic Charge-Density-Wave Behavior. *Angew. Chem., Int. Ed.* **2013**, *52*, 10477−10481.
(15) Pásztor, Á.; Scarfato, A.; Renner, C. Note: Mechanical in situ exfoliation of van der Waals materials. *Rev. Sci. Instrum.* **2017**, *88*, 076104.
(16) Feng, J.; Biswas, D.; Rajan, A.; Watson, M. D.; Mazzola, F.; Clark, O. J.; Underwood, K.; Marković, I.; McLaren, M.; Hunter, A.; et al. Electronic Structure and Enhanced Charge-Density Wave Order of Monolayer VSe_2. *Nano Lett.* **2018**, *18*, 4493−4499.
(17) Duvjir, G.; Choi, B. K.; Jang, I.; Ulstrup, S.; Kang, S.; Thi Ly, T.; Kim, S.; Choi, Y. H.; Jozwiak, C.; Bostwick, A.; et al. Emergence of a Metal-Insulator Transition and High-Temperature Charge-Density Waves in VSe_2 at the Monolayer Limit. *Nano Lett.* **2018**, *18*, 5432−5438.
(18) Chen, P.; Pai, W. W.; Chan, Y.-H.; Madhavan, V.; Chou, M. Y.; Mo, S.-K.; Fedorov, A.-V.; Chiang, T.-C. Unique Gap Structure and Symmetry of the Charge Density Wave in Single-Layer VSe_2. *Phys. Rev. Lett.* **2018**, *121*, 196402.
(19) Bonilla, M.; Kolekar, S.; Ma, Y.; Diaz, H. C.; Kalappattil, V.; Das, R.; Eggers, T.; Gutierrez, H. R.; Phan, M.-H.; Batzill, M. Strong room-temperature ferromagnetism in VSe_2 monolayers on van der Waals substrates. *Nat. Nanotechnol.* **2018**, *13*, 289−293.
(20) Cao, Q.; Yun, F. F.; Sang, L.; Xiang, F.; Liu, G.; Wang, X. Defect introduced paramagnetism and weak localization in two-dimensional metal VSe_2. *Nanotechnology* **2017**, *28*, 475703.
(21) Atkins, R.; Dolgos, M.; Fiedler, A.; Grosse, C.; Fischer, S. F.; Rudin, S. P.; Johnson, D. C. Synthesis and Systematic Trends in Structure and Electrical Properties of $[(SnSe)_{1.15}]_m(VSe_2)_1$, m = 1, 2, 3, and 4. *Chem. Mater.* **2014**, *26*, 2862−2872.
(22) Hite, O. K.; Falmbigl, M.; Alemayehu, M. B.; Esters, M.; Wood, S. R.; Johnson, D. C. Charge Density Wave Transition in $(PbSe)_{1+\delta}(VSe_2)_n$ Compounds with n = 1, 2, and 3. *Chem. Mater.* **2017**, *29*, 5646−5653.
(23) Falmbigl, M.; Fiedler, A.; Atkins, R. E.; Fischer, S. F.; Johnson, D. C. Suppressing a Charge Density Wave by Changing Dimensionality in the Ferecrystalline Compounds $([SnSe]_{1.15})_1(VSe_2)_n$ with n = 1, 2, 3, 4. *Nano Lett.* **2015**, *15*, 943−948.
(24) Lin, Q.; Smeller, M.; Heideman, C. L.; Zschack, P.; Koyano, M.; Anderson, M. D.; Kykyneshi, R.; Keszler, D. A.; Anderson, I. M.; Johnson, D. C. Rational Synthesis and Characterization of a New Family of Low Thermal Conductivity Misfit Layer Compounds $[(PbSe)_{0.99}]_m(WSe_2)_n$. *Chem. Mater.* **2010**, *22*, 1002−1009.
(25) Heideman, C. L.; Rostek, R.; Anderson, M. D.; Herzing, A. A.; Anderson, I. M.; Johnson, D. C. Synthesis and Electronic Properties of the Misfit Layer Compound $[(PbSe)_{1.00}]_1[MoSe_2]_1$. *J. Electron. Mater.* **2010**, *39*, 1476−1481.
(26) Fister, L.; Li, X. M.; McConnell, J.; Novet, T.; Johnson, D. C. Deposition system for the synthesis of modulated, ultrathin-film composites. *J. Vac. Sci. Technol., A* **1993**, *11*, 3014−3019.
(27) Hamann, D. M.; Bardgett, D.; Cordova, D. L. M.; Maynard, L. A.; Hadland, E. C.; Lygo, A. C.; Wood, S. R.; Esters, M.; Johnson, D. C. Sub-Monolayer Accuracy in Determining the Number of Atoms per Unit Area in Ultrathin Films Using X-Ray Fluorescence. *Chem. Mater.* **2018**, *30*, 6209−6216.
(28) Rodríguez-Carvajal, J. FULLPROF: A Program for Rietveld Refinement and Pattern Matching Analysis. In *Abstracts of the Satellite Meeting on Powder Diffraction of the XV Congress of the IUCr*: Toulouse, France, 1990; p 127.
(29) Toby, B. H. EXPGUI, a graphical user interface for GSAS. *J. Appl. Crystallogr.* **2001**, *34*, 210−213.
(30) Smeller, M. Structural Studies of $[(PbSe)_{0.99}]_m[WSe_2]_n$, $[(PbSe)_{1.00}]_m[MoSe_2]_n$, and $[(SnSe)_{1.03}]_m[MoSe_2]_n$ Misfit Layered Compounds. Ph.D. Dissertation, University of Oregon, Eugene, OR, 2011.
(31) Mariano, A. N.; Chopra, K. L. Polymorphism in Some IV-VI Compounds Induced by High Pressure and Thin-Film Epitaxial GROWTH. *Appl. Phys. Lett.* **1967**, *10*, 282−284.
(32) Schneemeyer, L. F.; Stacy, A.; Sienko, M. J. Effect of Nonstoichiometry on the Periodic Lattice Distortion in Vanadium Diselenide. *Inorg. Chem.* **1980**, *19*, 2659−2662.
(33) Zeppenfeld, A. C.; Fiddler, S. L.; Ham, W. K.; Klopfenstein, B. J.; Page, C. J. Variation of Layer Spacing in Self-Assembled Hafnium-1,10-Decanediylbis(Phosphonate) Multilayers As Determined by Ellipsometry and Grazing Angle X-Ray Diffraction. *J. Am. Chem. Soc.* **1994**, *116*, 9158−9165.
(34) Parratt, L. G. Surface Studies of Solids by Total Reflection of X-Rays. *Phys. Rev.* **1954**, *95*, 359−369.
(35) Cordova, D. L. M.; Kam, T. M.; Fender, S. S.; Tsai, Y. H.; Johnson, D. C. Strong Non-Epitaxial Interactions: Crystallographically Aligned PbSe on VSe 2. *Phys. Status Solidi A* **2019**, *216*, 1800896.
(36) Alemayehu, M. B.; Mitchson, G.; Ditto, J.; Hanken, B. E.; Asta, M.; Johnson, D. C. Charge Transfer between PbSe and $NbSe_2$ in $[(PbSe)_{1.14}]_m(NbSe_2)_1$ Ferecrystalline Compounds. *Chem. Mater.* **2014**, *26*, 1859−1866.
(37) Moore, D. B.; Beekman, M.; Zschack, P.; Johnson, D. C. Synthesis of Four New Members of the Ferecrystals. *2011 11th IEEE Conference on Nanotechnology*; IEEE-NANO, Aug 15−18, 2011; Vol. *16*, pp 1363−1366.
(38) Heideman, C. L.; Tepfer, S.; Lin, Q.; Rostek, R.; Zschack, P.; Anderson, M. D.; Anderson, I. M.; Johnson, D. C. Designed Synthesis, Structure, and Properties of a Family of Ferecrystalline Compounds $[(PbSe)_{1.00}]_m(MoSe_2)_n$. *J. Am. Chem. Soc.* **2013**, *135*, 11055−11062.
(39) Grosse, C.; Alemayehu, M. B.; Falmbigl, M.; Mogilatenko, A.; Chiatti, O.; Johnson, D. C.; Fischer, S. F. Superconducting Ferecrystals: Turbostratically Disordered Atomic-Scale Layered $(PbSe)_{1.14}(NbSe_2)_n$ Thin Films. *Sci. Rep.* **2016**, *6*, 33457.
(40) Atkins, R.; Moore, D. B.; Johnson, D. C. Insights into the Self-Assembly of Ferecrystalline Compounds from Designed Amorphous Precursors. *Chem. Mater.* **2013**, *25*, 1744−1750.
(41) Lin, Q.; Smeller, M.; Heideman, C. L.; Zschack, P.; Koyano, M.; Anderson, M. D.; Kykyneshi, R.; Keszler, D. A.; Anderson, I. M.; Johnson, D. C. Rational Synthesis and Characterization of a New

DOI: 10.1021/acs.chemmater.9b02826
Chem. Mater. 2019, 31, 8473−8483

Family of Low Thermal Conductivity Misfit Layer Compounds $[(PbSe)_{0.99}]_m(WSe_2)_n$. *Chem. Mater.* **2010**, *22*, 1002−1009.
(42) Anderson, M. D.; Heideman, C. L.; Lin, Q.; Smeller, M.; Kokenyesi, R.; Herzing, A. A.; Anderson, I. M.; Keszler, D. A.; Zschack, P.; Johnson, D. C. Size-Dependent Structural Distortions in One-Dimensional Nanostructures. *Angew. Chem., Int. Ed.* **2013**, *52*, 1982−1985.
(43) Eftekhari, A. Molybdenum diselenide ($MoSe_2$) for energy storage, catalysis, and optoelectronics. *Appl. Mater. Today* **2017**, *8*, 1−17.
(44) Bayard, M.; Sienko, M. J. Anomalous electrical and magnetic properties of vanadium diselenide. *J. Solid State Chem.* **1976**, *19*, 325−329.
(45) Heine, V. Theory of Surface States. *Phys. Rev.* **1965**, *138*, A1689−A1696.
(46) Dalven, R. A review of the semiconductor properties of PbTe, PbSe, PbS and PbO. *Infrared Phys.* **1969**, *9*, 141−184.
(47) Chattopadhyay, T.; Pannetier, J.; Von Schnering, H. G. Neutron Diffraction Study of the Structural Phase Transition in SnS and SnSe. *J. Phys. Chem. Solids* **1986**, *47*, 879−885.
(48) Falmbigl, M.; Alemayehu, M. B.; Merrill, D. R.; Beekman, M.; Johnson, D. C. In-Plane Structure of Ferecrystalline Compounds. *Cryst. Res. Technol.* **2015**, *50*, 464−472.
(49) Beekman, M.; Disch, S.; Rouvimov, S.; Kasinathan, D.; Koepernik, K.; Rosner, H.; Zschack, P.; Neumann, W. S.; Johnson, D. C. Controlling Size-Induced Phase Transformations Using Chemically Designed Nanolaminates. *Angew. Chem., Int. Ed.* **2013**, *52*, 13211−13214.

DOI: 10.1021/acs.chemmater.9b02826
Chem. Mater. 2019, 31, 8473−8483